Development of radially movable multichannel Reynolds stress probe system for a cylindrical laboratory plasma

Yoshihiko Nagashima,[1,a)] Shigeru Inagaki,[2] Kunihiro Kamakaki,[2] Hiroyuki Arakawa,[3] Takuma Yamada,[1] Shunjiro Shinohara,[4] Yoshinobu Kawai,[3] Masatoshi Yagi,[2] Akihide Fujisawa,[2] Sanae -I. Itoh,[2] Kimitaka Itoh,[5] and Yuichi Takase[1]

[1]*GSFS, The University of Tokyo, Kashiwa, Chiba 816-8561, Japan*
[2]*RIAM, Kyushu University, Kasuga, Fukuoka 816-8580, Japan*
[3]*IGSES, Kyushu University, Kasuga, Fukuoka 816-8580, Japan*
[4]*IE, Tokyo University of Agriculture and Technology, Koganei, Tokyo 184-8588, Japan*
[5]*National Institute for Fusion Science, Toki, Gifu 509-5292, Japan*

A new radially movable multichannel azimuthal probe system has been developed for measuring azimuthal and radial profiles of electrostatic Reynolds stress (RS) per mass density of microscale fluctuations for a cylindrical laboratory plasma. The system is composed of 16 probe units arranged azimuthally. Each probe unit has six electrodes to simultaneously measure azimuthal and radial electric fields for obtaining RS. The advantage of the system is that each probe unit is radially movable to measure azimuthal RS profiles at arbitrary radial locations as well as two-dimensional structures of fluctuations. The first result from temporal observation of fluctuation azimuthal profile presents that a low-frequency fluctuation (1–2 kHz) synchronizes oscillating Reynolds stress. In addition, radial scanning of the probe system simultaneously demonstrates two-dimensional patterns of mode structure and nonlinear forces with frequency $f = 1.5$ kHz and azimuthal mode number $m = 1$. © *2011 American Institute of Physics*. [doi:10.1063/1.3557384]

I. INTRODUCTION

Study of nonlinear dynamics of plasma turbulence is important for understanding energy transfer among multiscale turbulence and nonlinear saturation of turbulence and transport.[1] Recent theoretical progress has highlighted importance of secondary/tertiary instability/vortex excited by microscale turbulence.[2] The secondary/tertiary instabilities [i.e., zonal flows, streamers, convective cells, and general Kelvin–Helmholtz (GKH) instabilities] may be excited by nonlinear coupling with turbulence, even though they are linearly stable, and can affect the turbulence saturation backwardly. Therefore, coexistence of the secondary/tertiary instabilities and microscale turbulence is a key issue in understanding the saturation mechanism of the turbulence and turbulent transport. The excitation mechanism of the secondary instabilities may be momentum compression of turbulence fluctuation, and the compression can be measured through spatio-temporal dynamics of Reynolds stress (RS) per mass density of microscale fluctuation. In particular, the azimuthal gradient and/or curvature of the RS plays a significant role in excitation of the secondary instability with finite frequency and azimuthal wave number. A number of azimuthal probe arrays have been used to investigate the azimuthal structure of fluctuation in detail,[3–5] and energy exchange among fluctuations has been studied. In addition, previous work reported local measurements of energy transfer among fluctuations in frequency space.[6,7] However, homogeneity of the RS along the azimuthal direction at the same radial location is not guaranteed in turbulence, and simultaneous measurement of the RS in a wide azimuthal area is required. Other work tried to estimate energy flow direction between fluctuations by use of time delay from the amplitude correlation technique.[8] The amplitude correlation technique applied to scalar field fluctuations has the limitation that the technique can show only relative relationship between two modes and cannot provide any information on causality based on equation of motion. In order to clarify the causal relationship among fluctuations, direct observation of compression of energy/momentum is necessary. Therefore, measurement of the azimuthal profile of Reynolds stress is important to clarify the excitation mechanism of the secondary instability with finite azimuthal wave number. Recent work used the 128 channel fixed probe array to investigate energy transfer between turbulence and mean shear flow.[5] To investigate spatial structure of the secondary instabilities at an arbitrary radial location, an azimuthal probe array which is radially movable is required. To overcome the above problems on investigation of nonlinear energy transfer among multiscale turbulence, a new multichannel RS probe system has been installed on a linear device, the large mirror device-upgrade (LMD-U).[9] In this paper, we present a preliminary observation of drift-wave turbulence with the multichannel RS probe system as well as hardware details of the RS probe system. In LMD-U, a radially extended low-frequency oscillation propagating in the ion diamagnetic drift direction is observed at 1–2 kHz and is nonlinearly coupled to drift-wave turbulence.[10] In particular, we emphasize that we made the first real-time observation of direct energy exchange between the low-frequency oscillation and the RS of drift-wave turbulence. In addition, by radial scanning of the RS probe system, we have reconstituted two-dimensional
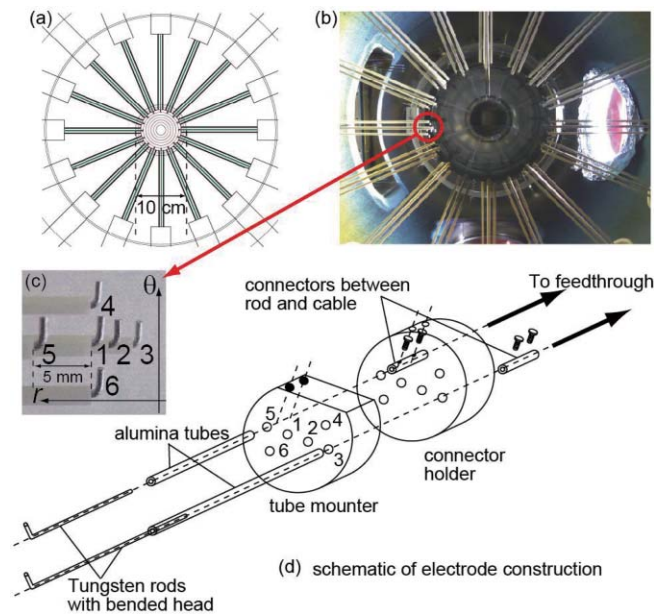
a)Electronic mail: nagashima@k.u-tokyo.ac.jp.

FIG. 1. (Color online) (a) Schematic view of multichannel Reynolds stress probe. (b) Photograph of the multichannel Reynolds stress probe during position calibration. (c) Enlarged photograph of six electrodes in a probe unit. In (c), vertical and horizontal arrows indicate the electron diamagnetic drift direction and radially outward direction, respectively. (d) Schematic view of probe construction. In (d), only electrode materials (rods and tubes) of #3 and #5 are illustrated for visibility.

patterns of mode structure and nonlinear forces from the turbulence. The patterns are uniquely obtained by the function of the radial mobility of the RS probe system. The measurement made by the diagnostic developed enables us to clarify causal relationships between modes and nonlinear forces and explore further nonlinear physics of plasma turbulence.

II. HARDWARE DESIGN AND CIRCUIT

The system is composed of 16 probe units arranged azimuthally [schematic view in Fig. 1(a) and photograph of arrangement in Fig. 1(b)] and can measure the RS with azimuthal mode structure up to $m \simeq 8$. Thus, the low-frequency fluctuation with the azimuthal mode number $m = 1$ is detectable. Each probe unit has six electrodes to simultaneously measure azimuthal and radial electric fields to obtain the RS, as shown in Fig. 1(c). All electrodes were used to measure the floating potential fluctuation $\tilde{\Phi}_f$ in this experiment. The $\tilde{\Phi}_f$ is an indicator of plasma potential fluctuation, assuming that the electron temperature fluctuation is negligible. (Poor electron temperature gradient in Ref. 11 suggests that the temperature fluctuation driven by fluctuating radial drift motion is very small.) A typical problem in the case of construction of a multichannel probe in a narrow area is a shadowing effect. When a number of electrodes are arranged nearly along the same magnetic field line, the shadowing effect by which $\tilde{\Phi}_f$ data are attenuated often occurs. To overcome the problem of the shadowing effect, the head of each tungsten electrode ($\phi = 0.8$ mm) is bent;[12] then we have confirmed there is no attenuation of $\tilde{\Phi}_f$ signals in this system.[13] We used four $\tilde{\Phi}_f$s to obtain Reynolds stress $-\langle \tilde{u}_r \tilde{u}_\theta \rangle = \langle \tilde{E}_\theta \tilde{E}_r / B^2 \rangle$. The azimuthal electric field fluctuation $\tilde{E}_\theta = -(\tilde{\Phi}_{f,4} - \tilde{\Phi}_{f,6})/d_\theta$ was

measured with a pair of electrodes (#4 and #6). The radial electric field fluctuation $\tilde{E}_r = -(\tilde{\Phi}_{f,5} - \tilde{\Phi}_{f,3})/d_r$ was measured with another pair of electrodes (#3 and #5), where the azimuthal electrode distance d_θ and radial electrode distance d_r are 10 mm. Electrode #1 is the basis of position calibration. In addition, we can estimate curvature of $\tilde{\Phi}_f$ by using three electrodes including electrode #1. For instance, radial curvature of $\tilde{\Phi}_f$ is measurable by use of the electrodes #1, #3, and #5. Electrode #2 is for multipurpose; checking aliasing in radial electric field measurement and measuring the ion saturation current for estimation of fluctuation driven particle flux.

A schematic view of probe construction is shown in Fig. 1(d). Small copper connectors ($\phi_{outer} = 2$ mm, $\phi_{inner} = 1$ mm) mounted inside the connector holder have the role of electrically connect electrodes (tungsten rod) to cables leading to multipin vacuum feedthrough. The vacuum feedthrough on the air side is connected to short semirigid coaxial cables ($\sim$60 cm), and the signal transmission lines are electrically shielded from one another. Ceramic (alumina) tubes are mounted at the tube mounter. The tube mounter has two screws per ceramic tube to stabilize and adjust the tube position across a Teflon tube. The position of the ceramic tube is minutely adjustable by the use of the two screws to specify contact area of the electrode to plasma, as shown in Fig. 1(c). Coaxial cables are not used in the signal transmission lines on the vacuum side, and each transmission line is not electrically shielded by the ground. Crosstalk among different signal transmission lines was investigated. We applied sinusoidal voltage waveform to five of the six signal transmission lines and measured the voltage at the remaining one line which is not applied by the sinusoidal waveform. The multipin feedthrough alone has crosstalk of $\sim$2% of the input voltage amplitude. Under condition of the full electrode installation, crosstalk is up to $\sim$5%, which is negligibly small.

The floating potential measurement requires that the electrode be electrically floated from the vessel ground by setting high impedance resistors in series. The 100 kΩ resistor (much larger than sheath impedance $\sim$300 Ω) is selected just after the semirigid cables. Then, long coaxial cables transmit $\tilde{\Phi}_f$ signals to low noise amplifiers (the gain of 40 dB and the delay time of 330 ns). Just before input of the amplifier, the long cables (8 m) are terminated by 50 Ω resister in order to effectively cancel capacitance of the long cable. Therefore, frequency response (especially phase delay) of the $\tilde{\Phi}_f$ measurement circuit mainly depends upon the capacitance of the semirigid cable. Typical phase delay is $\sim$5% at most at the ion cyclotron frequency $\leq$57 kHz ($B = 0.15$ T, maximum B in LMD-U experiment).

III. POSITION CALIBRATION

Arrangement of probes [Fig. 1(b)] was compared with stationary floating potential measurement. All the probe units are arranged at $\sim$4 cm radial location. The radius of 4 cm is almost the minimum radius where the full 16 probes can be installed at the same radial location. Previous work has shown that the two-dimentional profile of the stationary floating potential on an azimuthal cross section has a circular contour in LMD-U.[4] Based on the result, the #1
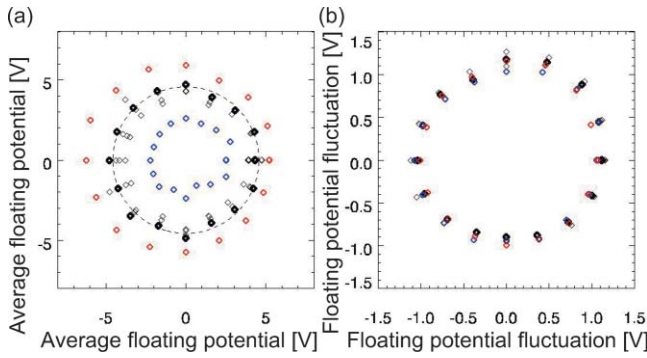
FIG. 2. (Color online) Examples of azimuthal profiles of floating potential. (a) Averaged floating potential profile, and (b) profile of averaged magnitude of floating potential fluctuation (1–30 kHz). Dashed line in (a) indicates azimuthal average of floating potential measured at #1 electrode in Fig. 1(c). Data observed at electrode #3 and #5 are shown in blue and red. Other electrodes are plotted in black. Symbols for #1 are thicker than others. Electrode #1 was set on the same stationary floating potential surface.
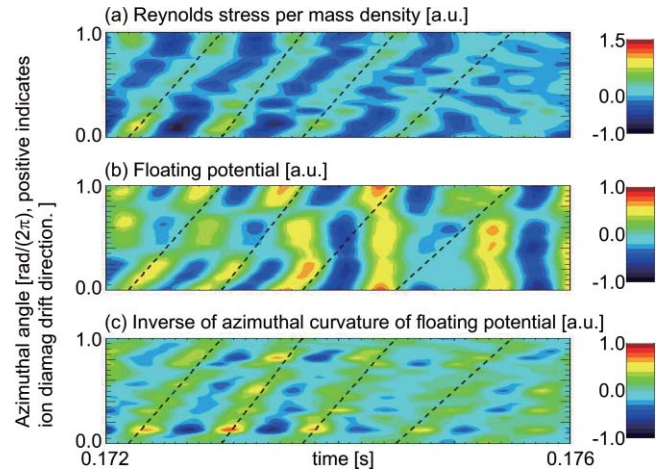

FIG. 3. (Color online) Time evolutions of fluctuation. (a) Reynolds stress per mass density, (b) floating potential, and (c) inverse of azimuthal curvature of floating potential. All waveforms are in frequency range of 1–2 kHz. Dashed lines are the guide to specify the same timing among waveforms (a)–(c). The azimuthal curvature of the floating potential synchronizes oscillation of the RS.

electrode is selected as the basis of azimuthal arrangement at the same radial location. Figure 2(a) shows the azimuthal polar plot of stationary floating potential obtained by all electrodes. Good arrangement was carried out for the #1 electrode. Considering the radial profile of the stationary floating potential,[14] variance of the floating potential of the #1 electrode among the 16 probe units indicates less than a few millimeters of radial variance of position calibration. On the contrary, centers of the floating potential 180 plots of #3 (innermost) and #5 (outermost) electrodes are shifted from the center of the polar plot. These shifts may be caused by divergence of the plasma center from the center of the vacuum vessel. The multichannel RS probe system is mounted on flanges of the vacuum vessel, and there is a discrepancy in the angles of probe insertion line from the normal line of the same floating potential contour. The discrepancy can be calibrated and does not significantly affect the azimuthal profile of the RS. In contrast to the stationary floating potential, there is no significant difference among $\tilde{\Phi}_f$ amplitudes (1–30 kHz) of the six electrodes in a probe unit and among those of 16 probe units. Nonlinear momentum/vorticity transfer may be caused by amplitude gradient and/or phase difference between fluctuations. This uniformity of fluctuation amplitude around the radial location suggests that nonlinear momentum/vorticity transfer between fluctuations may be predominantly caused not by amplitude gradient of the scalar fields but by phase relationship between fluctuations or amplitude gradient of vector fields.

IV. AZIMUTHAL PROFILES OF MODE AMPLITUDE AND OSCILLATING REYNOLDS STRESS

In LMD-U, the radially extended secondary instability ($f \sim 1-2$ kHz, $m = 1$) propagating in the ion diamagnetic drift direction has been studied. The excitation mechanism of the instability has not been concluded in terms of nonlocal effect and causality (i.e., momentum/vorticity equations). Based on a simple one-field model, the excitation mechanism of the tertiary general Kelvin–Helmholtz instability associated with the secondary

zonal flow instability is presented as Eq. (3.4.1) in Ref. 2. Without the zonal flow instability and the GKH driven by the zonal flow, the secondary vortex flow can be generated via a modulational instability of turbulence. In this case, the vorticity equation for the secondary vortex flow generation by microscale fluctuation is written as [Eq. (6.1.4) in Ref. 15],

$$\frac{\partial}{\partial t}\langle\Delta\phi\rangle = \left(\frac{\partial^2}{\partial x^2} - \frac{\partial^2}{\partial y^2}\right)\langle\tilde{V}_x\tilde{V}_y\rangle + \frac{\partial^2}{\partial x \partial y}\left(\langle\tilde{V}_x^2\rangle - \langle\tilde{V}_y^2\rangle\right), \quad (1)$$

where $\tilde{V}_x$ and $\tilde{V}_y$ are radial and azimuthal velocity fluctuations, respectively. In Eq. (1), the shear stress is a key mechanism behind excitation of the secondary vortex flow. On the right hand side of Eq. (1), the first and second terms are driving terms by the Reynolds stress of turbulence and by gradient of momentum compression of turbulence, respectively. Concerning the first term, the Reynolds stress (off-diagonal term of Lagrangian nonlinearity) is the radial flux of the azimuthal momentum and/or the azimuthal flux of the radial momentum, linking directly to the shear stress. When the radial gradient/curvature of the RS is not the same as the azimuthal ones, vortex flow acceleration force residues, then the secondary vortex flows can be excited. Zonal flows or streamers can be excited in the limit to the case that the azimuthal or radial gradient/curvature of the RS is negligible. Concerning the second term, compression of the momentum may occur when diagonal terms of Lagrangian nonlinearity have finite gradient in the direction same as the momentum. Then compression of the momentum may have the gradient in the direction perpendicular to the accumulated momentum; the shear stress appears and can drive the secondary vortex flow.

First, we show visual plots of spatio-temporal behaviors of fluctuation dynamics, mode components, and nonlinear force. Figure 3 shows an example of time evolutions of azimuthal profiles of three quantities, the RS, the floating potential, and inverse of azimuthal curvature of floating potential. The radial and azimuthal electric field fluctuations (1–30 kHz) are obtained, and the RS is calculated by product
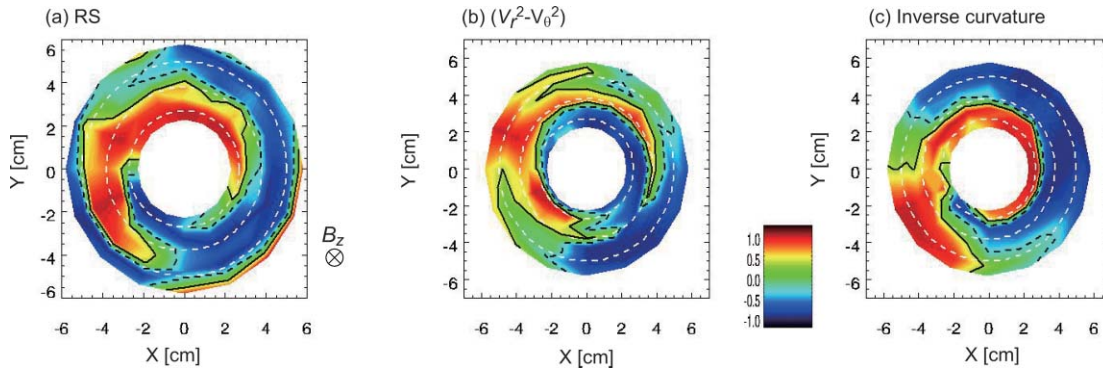
FIG. 4. (Color online) Two-dimensional patterns of fluctuations at 1.5 kHz. Cross-phase (Θ) pattern of (a) $-(\tilde{u}_r \tilde{u}_\theta)$ (Reynolds stress per mass density), (b) $(\tilde{u}_r^2 - \tilde{u}_\theta^2)$, and (c) $-\nabla^2 \Phi_f$ (inverse of curvature of floating potential) are plotted. The cross-phases are estimated from cross-spectra averaged over $\sim$1000 data windows obtained under the same operation condition. In each contour, $\cos \Theta$ is plotted for clarity. The cross-phases are calculated between the RS data at fixed locations and the three physical quantities scanned radially. Solid and dashed lines in black indicate contour lines at ± 0.25. Three dashed circular lines in white indicate three different radial locations, $r = 2.7, 3.8, 5.0$ cm, for guide of view, respectively. Basically, mode structures with $m = 1$ are clearly observed in the three contours.

of the electric field fluctuations. Experimental conditions are almost the same as in Ref. 11. All waveforms are in the frequency range of 1–2 kHz. In Fig. 3(a), modulation of the Reynolds stress with mode number of $m = 1$ propagates in the ion diamagnetic drift direction. On the contrary, time evolution of the floating potential in Fig. 3(b) is complicated. The spatiotemporal profile of the floating potential is composed of many wave number components including $m = 0$. In order to distinguish the secondary instability with $m = 0$ from other wave number components, azimuthal curvature of the floating potential is shown in Fig. 3(c). Structure with azimuthal mode of $m = 1$ can be clearly seen, and the azimuthal curvature is synchronized with the Reynolds stress. This observation indicates that the mode structure with $m = 1$ is temporally correlated with the nonlinear force (Reynolds stress) at $\sim$4 cm.

V. TWO-DIMENSIONAL PATTERNS OF MODE STRUCTURE AND NONLINEAR FORCES

The combination of the radial scan of the RS probe and the correlation technique can reconstitute two-dimensional patterns of not only linear mode structures of fluctuations but also nonlinear force driven by the fluctuations. The radial scan is the advantage of the probe system compared with previous work. Next, we show the two-dimensional patterns of $-\tilde{u}_r \tilde{u}_\theta$ (the RS), $(\tilde{u}_r^2 - \tilde{u}_\theta^2)$ [the part of the second term on the right hand side of Eq. (1)], and $-\nabla^2 \Phi_f$ (the inverse curvature of the floating potential). Figure 4 demonstrates the cross-phase Θ spectra of the fluctuations, shown as $\cos \Theta$. The cross-phases are calculated between the RS data at fixed locations and the three physical quantities scanned radially. Basically, mode structures with $m = 1$ dominate in the three contours, and the patterns are correlated well with the RS. Curvature of the RS on the right hand side of Eq. (1) is the force to excite the potential vorticity on the left hand side of Eq. (1). Therefore, energy exchange between the RS and the vorticity is statistically admissible. As shown in Fig. 4(b), the second term on the right hand side of Eq. (1) may also affect the mode structure with $m = 1$. However, radial

structures of the $m = 1$ modes are complicated. For instance, in the field between $r = 5.0$ and 3.8 cm in the RS contours (Fig. 4), areas of positive and negative amplitude region are not equal. This indicates that the $m = 1$ mode pattern has an offset of $m = 0$ structure that also oscillates at 1–2 kHz. In Fig. 3(b), the floating potential structure of $m = 0$ can be seen. When the $m = 0$ structure has finite radial wave number, the structure could be an zonal flow structure.

The combination of the radial scanning of the RS probe system and the correlation technique, the two-dimensional relationship between the mode structure and nonlinear forces was clearly observed, leading to understanding of stationary force balance behind the turbulence observed. Furthermore, simultaneous measurement of spatio-temporal mode structure and nonlinear forces could explore research on the nonstationary turbulence.

In future work, radial gradient/curvature of the off-diagonal RS term [the first term on the right hand side of Eq. (1)] and gradient/curvature of diagonal momentum transfer [the second term on the right hand side of Eq. (1)] would be precisely taken into account to confirm excitation mechanism of the secondary instability/vorticity by microscale fluctuations.

ACKNOWLEDGMENTS

[1] A. Yoshizawa, S.-I. Itoh, and K. Itoh, *Plasma and Fluid Turbulence: Theory and Modelling* (Institute of Physics, Bristol, 2003).

[2] P. Diamond, S.-I. Itoh, K. Itoh, and T. Hahm, Plasma Phys. Controlled Fusion **47**, R35 (2005).

[3] A. Latten, T. Klinger, and A. Piel, Rev. Sci. Instrum. **66**, 3254 (1995).

[4] T. Yamada, Y. Nagashima, S. Inagaki, Y. Kawai, M. Yagi, S.-I. Itoh, T. Maruta, S. Shinohara, K. Terasaka, M. Kawaguchi, M. Fukao, A. Fujisawa, and K. Itoh, Rev. Sci. Instrum. **78**, 123501 (2007).

[5] P. Manz, M. Ramisch, and U. Stroth, Phys. Plasmas **16**, 042309 (2009).

[6] M. Xu, G. R. Tynan, C. Holland, Z. Yan, S. H. Muller, and J. H. Yu, Phys. Plasmas **17**, 032311 (2010).

[7] Y. Nagashima, S.-I. Itoh, S. Shinohara, M. Fukao, A. Fujisawa, K. Terasaka, Y. Kawai, G. R. Tynan, P. H. Diamond, M. Yagi, S. Inagaki, T. Yamada, and K. Itoh, Phys. Plasmas **16**, 020706 (2009).

[8] H. Xia and M. Shats, Phys. Rev. Lett. **91**, 155001 (2003).

[9] K. Terasaka, S. Shinohara, Y. Nagashima, T. Yamada, M. Kawaguchi, T. Maruta, S. Inagaki, Y. Kawai, N. Kasuya, M. Yagi, A. Fujisawa, K. Itoh, and S.-I. Itoh, J. Plasma Fusion Res. **2**, 31 (2007).

[10] T. Yamada, S.-I. Itoh, T. Maruta, N. Kasuya, Y. Nagashima, S. Shinohara, K. Terasaka, M. Yagi, S. Inagaki, Y. Kawai, A. Fujisawa, and K. Itoh, Nat. Phys. **4**, 721 (2008).

[11] T. Yamada, S.-I. Itoh, S. Inagaki, Y. Nagashima, S. Shinohara, N. Kasuya, K. Terasaka, K. Kamataki, H. Arakawa, M. Yagi, A. Fujisawa, and K. Itoh, Phys. Plasmas **17**, 052313 (2010).

[12] N. Krause, C. Lechte, J. Stöber, U. Stroth, E. Ascasibar, J. Alonso, and S. Niedner, Rev. Sci. Instrum. **73**, 3474 (2002).

[13] Y. Nagashima, S.-I. Itoh, K. Itoh, A. Fujisawa, S. Inagaki, Y. Kawai, S. Shinohara, M. Fukao, T. Yamada, K. Terasaka, T. Maruta, K. Kamataki, H. Arakawa, M. Yagi, N. Kasuya, G. R. Tynan, P. H. Diamond, and Y. Takase, J. Plasma Fusion Res. **8**, 0050 (2009).

[14] H. Arakawa, S. Inagaki, Y. Nagashima, T. Yamada, K. Kamataki, T. Kobayashi, S. Sugita, M. Yagi, N. Kasuya, A. Fujisawa, S.-I. Itoh, and K. Itoh, Plasma Phys. Controlled Fusion **52**, 105009 (2010).

[15] P. Diamond, S.-I. Itoh, K. Itoh, and T. Hahm, NIFS Report No. NIFS-805, National Institute for Fusion Science, 2004.